Modeling of microwave magnetic envelope solitons in thin ferrite films through the nonlinear Schrödinger equation

Hong Yan Zhang,[a] Pavel Kabos,[b] Hua Xia, Reinhold A. Staudinger, Pavel A. Kolodin, and Carl E. Patton
Department of Physics, Colorado State University, Fort Collins, Colorado 80523

(Received 11 May 1998; accepted for publication 7 July 1998)

A theoretical analysis of microwave magnetic envelope soliton profiles and the soliton peak power response for high power magnetostatic wave (MSW) excitations in yttrium iron garnet (YIG) thin films has been made. This analysis was based on the standard nonlinear Schrödinger equation with all key parameters based on experiment. The measurements were done for magnetostatic backward volume waves in a 10.2 μm YIG film, with a band edge at 5.06–5.07 GHz and operating point frequencies from 4.80 to 5.00 GHz. The use of accurate dispersion and group velocity parameters and the transmitted power versus frequency response of the MSW signal was critical. It was possible to accurately model both the shapes of the soliton pulses and the peak output versus peak input power response over a wide range of power levels. © *1998 American Institute of Physics.* [S0021-8979(98)07219-3]

I. INTRODUCTION

By far the largest effort concerning solitons has been in the area of nonlinear optics.[1] In the last decade or so, however, the availability of high-quality, narrow linewidth single-crystal thin films of yttrium iron garnet (YIG) for microwave signal-processing applications, as well as advanced instrumentation for microwave pulse generation, detection, and analysis, has led to a growing interest in microwave magnetic envelope (MME) solitons.[2–17] Such MME solitons have been observed in YIG films with various surface pinning condition and magnetized in different magnetic field configurations.

The analysis of soliton properties is often done through various nonlinear differential equations. An excellent review of these approaches is provided by Hasegawa.[1] The equation of choice for the analysis of envelope solitons is the so-called nonlinear Schrödinger (NLS) equation.[18] The NLS equation has been used to model a wide variety of MME soliton properties. These include soliton profiles and decay,[9] phase properties of dark solitons,[10,17] profile shapes and peak power response,[11] energy decay,[15] and power thresholds for the formation of solitons of different order.[14,16] The modeling results on decay and phase are in reasonable agreement with experiment. However, up to now, the pulse profiles and peak power response curves obtained from the NLS modeling have not matched the results of the experiments.[11]

The objective of this work was to perform a critical study of MME soliton profiles and the soliton peak power response based on the NLS equation and with all relevant parameters tied directly to experiment. The MME pulse propagation parameters were determined from transmission loss versus frequency and propagation time measurements at low power levels. The simulations were based on the NLS equation and a Fourier analysis procedure to account for frequency cutoff effects associated with the magnetostatic wave (MSW) band edge. It was possible to obtain theoretical pulse profiles and power response curves which were in good agreement with experiment. The use of (i) accurate dispersion and pulse velocity parameters and (ii) filtering to account for the frequency response of the MSW transmission was critical to these good fits.

Section II presents the details of the measurement techniques and experimental results for both low and high power. Section III introduces the basic NLS model to describe MME soliton propagation and describes the effect of parameter variations and band edge effects on calculated peak power response curves and pulse profiles. Section IV presents comparisons of computed power response curves and pulse profiles with experiment.

II. THE EXPERIMENT

The setup for the generation and detection of MSW signals is shown in Fig. 1. The microwave source provides input cw or pulse power to the input antenna at point A. The YIG film strip is magnetized by an in-plane static magnetic field along the propagation direction. This configuration corresponds to the magnetostatic backward volume wave (MSBVW) configuration. The output antenna signal at B is then detected and analyzed. The YIG film strip and the two antennas shown in Fig. 1 will be denoted as the YIG film transducer structure.

The details of the microwave and signal analysis electronics are given in Ref. 15. The cw experiments at low power utilized a standard microwave synthesizer as the signal source. For the high power pulse experiments, the synthesizer signal was fed to a high speed microwave switch and a microwave amplifier. The output signals in the cw experi-

[a]On leave from the Pohl Institute of Solid-State Physics, Tongji University, Shanghai 200092, People's Republic of China; electronic mail: hongyan@lamar.colostate.edu
[b]On leave from the Faculty of Electrical Engineering and Information Technology of the Slovak Institute of Technology, Bratislava, Slovakia.

 © 1998 American Institute of Physics

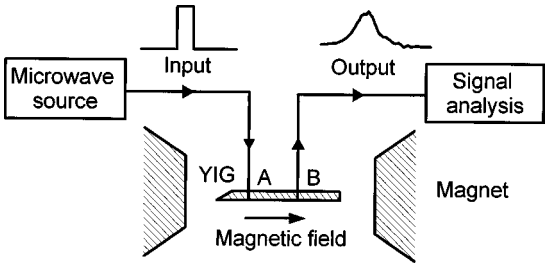

FIG. 1. Schematic illustration of the measurement system. The microwave source provides cw or pulse microwave excitation to the input transducer, labeled A, near the left end of the yttrium iron garnet (YIG) film strip. The signal from the output transducer at B is then processed by the signal analysis electronics. A magnetic field is applied parallel to the long direction of the YIG strip.

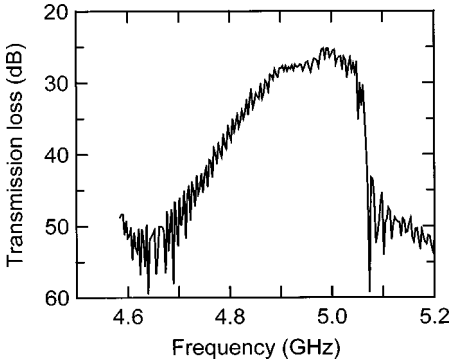

FIG. 2. Low power transmission loss vs frequency for YIG film transducer structure in the MSBVW configuration. The input cw microwave power was 1 mW.

ments were analyzed with an HP 8510C Network Analyzer. For the pulse experiments, the input pulse width was 13 ns for all of the results given below, and the propagated signal at the output transducer was detected and analyzed with an HP 71500A microwave transition analyzer (MTA).

The YIG film transducer structure consisted of two 50 μm wide microstrip transducers across a long and narrow 1.5 mm$\times$20 mm YIG film strip. For all of the data and modeling results shown below, the transducer separation was held fixed at 4 mm. The 10.2 μm thick single-crystal (111) YIG film was grown by standard liquid phase epitaxy techniques on gadolinium galium garnet. The film was provided by Dr. J. Douglas Adam, Northrop Grumman, Inc. The film was magnetized by an external static magnetic field of 1187 Oe.

The magnetic properties of the YIG film, in combination with the MSBVW configuration and the static magnetic field chosen for the experiment, determine various parameters which will be critical for the measurements and the analysis to follow. The saturation induction $4\pi M_s$ of the YIG material will be taken at the nominal literature value of 1750 G. The absolute value of the gyromagnetic ratio, denoted as γ, is taken at the free electron value of 1.76×10^6 rad/Oe s or, in practical units, 2.8 GHz/kOe. The microwave loss of the YIG film is characterized by a measured ferromagnetic resonance (FMR) half power linewidth of 0.9 Oe at 5 GHz.

Representative data on the MSBVW cw signal transmission loss versus frequency are given in Fig. 2. The cw input power was about 1 mW. The film parameters and experimental conditions are the same as given above. These data show two important features. First, there is a sharp cutoff at a high-frequency band edge around 5.06–5.07 GHz. Second, the transmission curve over the frequency interval from about 4.85 to 5.05 GHz is relatively flat. This plateau region will be used for the pulse measurements at different frequencies to be considered shortly. The situation here is similar to the conditions for the MSBVW soliton experiments of Ref. 11 for a 7.2 μm thick films. The transmission loss versus frequency results in Fig. 2 will also be used to filter the Fourier transform of calculated MME pulse profiles in Sec. III.

Based on the transmission loss versus frequency profile in Fig. 2, pulse measurements at low and high power were made over the plateau region from about 4.80 to 5.05 GHz. The evolution of the pulse shape with frequency, for a fixed input pulse width and relatively low input power levels, demonstrated the effect of a frequency-dependent dispersion on these shapes. From further measurements of delay time versus frequency at low power, values of the group velocity and dispersion coefficient as a function of frequency could be determined. These parameters and, in particular, their variations with frequency, will be important for the NLS equation based modeling to be considered in Secs. III and IV. The high power measurements over the plateau region consisted of (i) output profiles and (ii) peak output power versus peak input power response curves. Section IV will present computed profiles and response curves for direct comparison with these data.

Some representative output profile data for an input pulse width of 13 ns and an input peak power of 150 mW are shown in Fig. 3. The operating point frequencies ranged from 4.85 GHz for the bottom graph to 5.05 GHz for the top

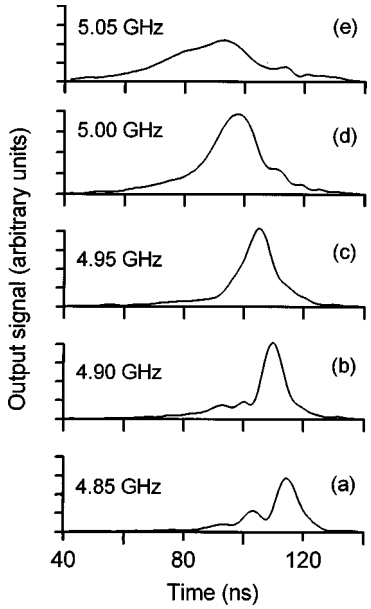

FIG. 3. Output pulse MTA signal voltage vs time for different operating point frequencies, as indicated. The vertical scales are the same for all graphs. The input peak power was 150 mW.

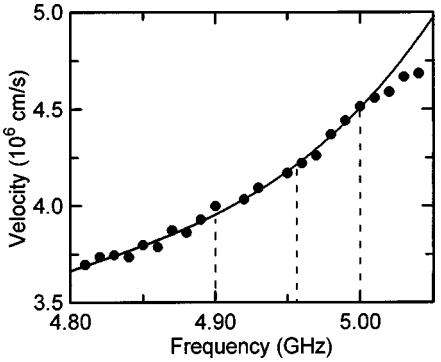

FIG. 4. Velocity as a function of frequency for low power MSBVW pulses formed from 13 ns wide input pulses with a peak power of 150 mW. The data shown are based on propagation time measurements.

graph, as indicated. This span of frequencies matches the plateau region in Fig. 2. The data shown are for the detected MTA voltage versus time. The vertical scales are the same for all graphs. The most striking aspect of the pulse profiles in Fig. 3 is the significant broadening which occurs as one moves from the low frequency end of the plateau region at 4.85 GHz for (a) to the upper end at 5.05 GHz for (e). The change from (a) to (c) is more-or-less gradual, and then there is a doubling in width from (c) to (e). The gradual broadening in the pulse profiles from (a) to (c) is due to the increase in dispersion with frequency. The larger change from (c) to (e) is exacerbated by the proximity of the operating point frequency to the band edge frequency at 5.06–5.07 GHz evident from Fig. 2. These effects will be considered in more detail below.

It is also important to note that the peak positions for the profiles in Fig. 3 shift down in time with increasing frequency. These shifts correspond to an increase in the pulse velocity with frequency. Accurate measurements of the propagation time, in combination with the 4 mm transducer spacing for the experiment, were used to determine the low power MME pulse group velocity versus frequency. These data, in turn, were used to make quantitative determinations of the dispersion as a function of frequency.

The results of these propagation time measurements are shown in Fig. 4. The figure shows pulse velocity as a function of frequency over the range 4.80–5.05 GHz, the plateau part of the passband previously noted. The solid circles show the data. The solid curve shows a smoothed fit to the data with the points above 5.00 GHz excluded. The three vertical dashed lines indicate special frequency points at 4.90, 4.96, and 5.00 GHz. These frequencies will be important for the measurements and the NLS equation based simulations.

The data in Fig. 4 quantify the decrease in propagation time with increasing frequency evident from the shift in pulse position with frequency in Fig. 3. These data demonstrate the increase in velocity with frequency. Below 5 GHz, the rate of increase in the pulse velocity with frequency also increases. Above 5 GHz, there is a falloff in the rate of increase. This falloff is related to the fact that, as one moves above 5 GHz, one is also approaching the band edge. The apparent falloff in velocity in this range is connected to the large distortion in pulse shape which occurs in this region and shown in Fig. 3(e).

The data in Fig. 3 and Fig. 4 are representative of the pulse shape and velocity frequency dependences for power levels below those for which soliton considerations become important. The results, however, have important consequences for MME soliton experiments and the modeling of these experiments. The key effect has to do with dispersion. The velocity value for a given point in Fig. 4 corresponds to the low power group velocity ν_g for the measured pulse. The measured slope of the velocity versus frequency response, in combination with ν_g, may be used to determine the dispersion. The fact that this slope is an increasing function of frequency indicates that the dispersion is also increasing with frequency.

Now turn to the analysis of the Fig. 4 data to obtain the applicable dispersion parameters for the experiment and the modeling to follow. The group velocity for an MME wave packet is defined by

$$\nu_g = \left.\frac{\partial \omega}{\partial k}\right|_o , \tag{1}$$

where ω and k are the carrier angular frequency and wave number of the packet, respectively. The units of ω and k are rad/s and rad/cm, respectively. The ''o'' indicates that the derivative expression for ν_g is to be evaluated at some specified operating point frequency and wave number on the dispersion curve for the plane wave excitation of interest.

The dispersion is usually defined in terms of the change of the group velocity with respect to wave number and expressed through a dispersion coefficient D:

$$D = \left.\frac{\partial^2 \omega}{\partial k^2}\right|_o . \tag{2}$$

In order to obtain values of D as a function of frequency from the data of Fig. 4, it is convenient to rewrite Eq. (2) in the form

$$D = \frac{\partial}{\partial k}\left(\frac{\partial \omega}{\partial k}\right) = \left(\frac{\partial \omega}{\partial k}\right)\left[\frac{\partial}{\partial \omega}\left(\frac{\partial \omega}{\partial k}\right)\right] = \nu_g \frac{\partial \nu_g}{\partial \omega}. \tag{3}$$

The ''o'' nomenclature has been left out of Eq. (3), but the same considerations apply. Based on Eq. (3), the velocity points on the solid curve in Fig. 4 and the slope of the curve at these points may be used to obtain D as a function of frequency. A practical form of Eq. (3) was used to analyze the data:

$$D(\mathrm{cm^2/rad\ s}) = \frac{10^{-9}}{2\pi}\left[\nu_g(\mathrm{cm/s})\right]\left[\frac{\Delta \nu_g(\mathrm{cm/s})}{\Delta f(\mathrm{GHz})}\right]. \tag{4}$$

The $\Delta \nu_g$ and Δf in Eq. (4) denote increments in velocity and frequency, respectively, based on the slope of the solid curve in Fig. 4 at the frequency of interest.

Table I lists values of the group velocity ν_g and the dispersion parameter D obtained from the solid curve in Fig. 4 and Eq. (4) for four frequencies, 4.83, 4.90, 4.96, and 5.00 GHz. The results show the effects noted above. These is a modest increase in the group velocity with frequency. Most important, however, is the rather large change in the disper-

TABLE I. Group velocity ν_g and dispersion parameter D at different frequencies.

Frequency	4.83 GHz	4.90 GHz	4.96 GHz	5.00 GHz
ν_g (cm/s)	3.78×10^6	3.94×10^6	4.23×10^6	4.48×10^6
D (cm^2/rad s)	1055	2656	3735	4708

sion parameter with frequency. Note that D changes by almost a factor of 2 from 4.90 to 5.00 GHz. The changes in ν_g and D with frequency will have an important effect on computed soliton properties to be considered in the next section.

Now that the basic experimental procedures have been established, and the effect of operating point frequency on pulse shape, group velocity, and dispersion has been determined, the remainder of this section will consider actual data on pulse profiles and output pulse peak power versus input pulse peak power response. Data are presented below for the frequencies in the three right most columns in Table I and marked by the vertical dashed lines in Fig. 4, 4.90, 4.96, and 5.00 GHz. These frequencies were selected in order to (i) examine the effect of D on the soliton response properties and (ii) examine the effect, if any, of a carrier frequency close to the band edge. Note that 5.00 GHz is 60–70 MHz from the MSBVW band edge. This is the same order as the width in the frequency spectrum for the 13 ns wide input pulse used to obtain the results in Fig. 3.

Some representative profile data for 4.90 GHz are shown in Fig. 5 for input pulse peak power levels from 5 to 307 mW. Other experimental parameters were the same as for Fig. 3. Power versus time profiles for both the input and output pulses are given for four increasing values of the peak input power, as indicated. For better resolution, the profiles

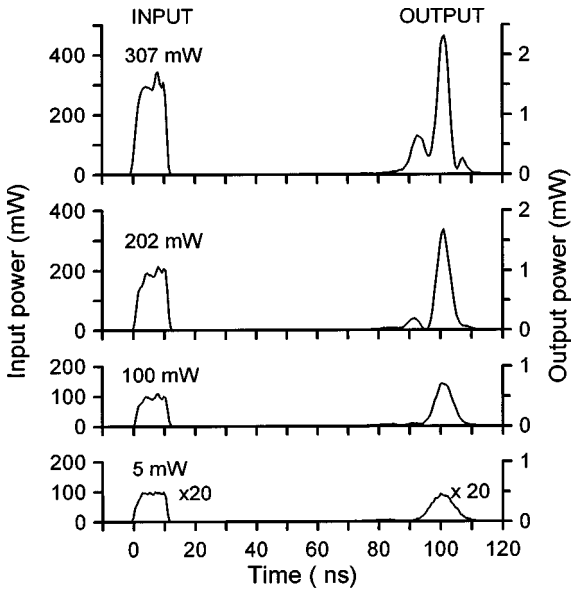

FIG. 5. Input and output power vs time for different input pulse peak power values, as indicated. The signal carrier frequency was 4.9 GHz. The traces for the 5 mW input power graph are shown on an expanded vertical scale by a factor of 20.

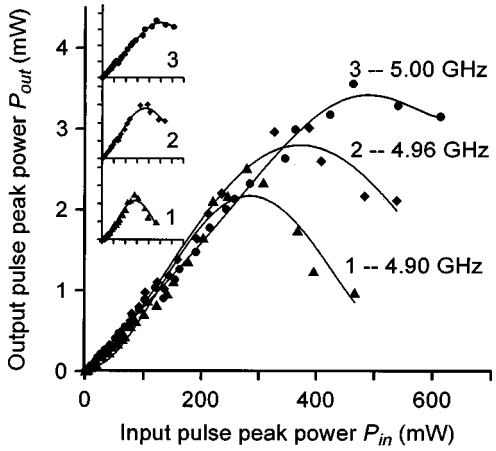

FIG. 6. Output pulse peak power P_{out} vs input pulse peak power P_{in} for three operating point frequencies, as indicated. The inset graphs show the three sets of data separately. The solid lines are a guide to the eye.

for the 5 mW input peak power are expanded by a factor of 20. The output power profiles here are similar to previously published data.[10] Figure 5 shows that the output profiles steepen and narrow as the power is increased. In addition, the profile at the highest power shows multiple peaks indicative of higher order soliton behavior.

The output profile results for the other frequencies were qualitatively similar but with some important and subtle differences. At the near band edge frequency of 5.00 GHz, for example, the profiles did not show as much steepening and narrowing as evident in Fig. 5, and the development of multiple peaks was suppressed. These output profile data will be revisited in Sec. IV and compared with results from modeling based on the NLS equation.

Now turn to the results on the output pulse peak power versus input pulse peak power response. Figure 6 shows representative data for the three frequencies noted above and as indicated. The input pulse peak power and the output pulse peak power are denoted as P_{in} and P_{out}, respectively. Other experimental parameters were the same as for Fig. 5. The inset curves show the same data separately in order to make clear the differences in shapes for the three responses. The solid lines through the data points are intended as a guide to the eye only. They do not represent theoretical results.

The main effects of the change in frequency on the power response profiles in Fig. 6 are evident from the upward and outward shift in the maximum P_{out} response as the frequency is increased from curve 1 to curve 2 to curve 3. Besides these changes, there are also differences in the shapes of the curves which can be more clearly seen from the insets. For curve 1, the onset of the initial nonlinear response takes place close to $P_{\text{in}}=100$ mW. For curve 2, the nonlinear response is not as pronounced as for curve 1. The onset of the nonlinear behavior is close to $P_{\text{in}}=200$ mW, but is barely discernable in the Fig. 6 inset. Curve 3 shows no clear nonlinear response onset at all, and the drop in P_{out} above 400–500 mW is much less pronounced.

As will be evident in Sec. IV, all of these changes are related to the changes in velocity and dispersion with frequency, and cutoff effects related to the approach to the band

edge. As a rule, the increase in v_g with frequency causes the peak response to move to higher P_{out} values, the increase in D causes the peak position to shift to higher P_{in} values, and the frequency approach to the band edge tends to smooth out sharp features of the response.

III. THE MODEL

The objective here is to model MME soliton profiles and the soliton peak power response based on the NLS equation, with the soliton parameters which go into the model obtained directly from experiment. Now that experimental values of v_g and D have been determined, and both experimental profiles and peak power response curves have been obtained, the NLS equation based modeling may be considered in more detail.

First, one uses the NLS equation with a reconstructed spatial input pulse to obtain time-dependent output pulse profiles. Second, the Fourier transforms of these output pulses are filtered according to the transmission loss versus frequency characteristic found experimentally in Fig. 2 and further reconstructed output pulse profiles are obtained for comparison with experiment.

The formulation given below follows the notation of Ref. 11. Consider an MSBVW wave packet with a propagation direction along the positive z axis and a dynamic magnetization response $\mathbf{m}(z,t)$ of the form

$$\mathbf{m}(z,t)=\mathbf{m}_{\text{env}}(z,t)e^{-i(kz-\omega_k t)}. \tag{5}$$

The z direction is along the long direction of the YIG strip shown in Fig. 1. The dynamic magnetization $\mathbf{m}(z,t)$, to lowest order, has only in-plane and out-of-plane components perpendicular to this z direction. As in Ref. 11, one may define a dimensionless, reduced, and complex scalar wave packet envelope function $u(z,t)$ which is related to the dynamic magnetization envelope function $\mathbf{m}_{\text{env}}(z,t)$. Here, as Ref. 11, this connection will be written as

$$\mathbf{m}_{\text{env}}^{(\text{in})}(z,t)=u(z,t)M_s, \tag{6}$$

where $\mathbf{m}_{\text{env}}^{(\text{in})}(z,t)$ is the wave packet envelope function associated with the in-plane component of the dynamic magnetization response. Under the conditions of the experiments of the previous section, the ratio $\mathbf{m}_{\text{env}}^{(\text{in})}/M_s$ is typically in the range of 1%–10%.

The standard procedure has been to model MME solitons through the one-dimensional nonlinear Schrödinger equation:

$$i\left(\frac{\partial u}{\partial t}+v_g\frac{\partial u}{\partial z}+\eta u\right)+\frac{1}{2}D\frac{\partial^2 u}{\partial z^2}-N|u^2|u=0. \tag{7}$$

The parameters and the notation are the same as in Ref. 11. The u parameter refers to complex $u(z,t)$ envelope function defined above. The v_g and D parameters are the same as in Sec. II. The η parameter takes energy loss or damping into account. For the YIG film FMR linewidth of 0.9 Oe cited in Sec. II, the corresponding value of η is 7.9×10^6 rad/s. The N parameter describes the frequency shift of the MSW excitation as the size of the dynamic magnetization amplitude is increased. The N parameter is usually defined according to $N=\partial\omega/\partial|u|^2$, where ω is the operating point carrier frequency from Sec. II and the derivative is evaluated at $|u|^2=0$. The evaluation of N is considered in detail in Ref. 11. For the modeling results to be given below, N will be taken to be 6.85×10^9 rad/s. This value follows from Eq. (9) of Ref. 10 for MSBVW excitations, the definition of $u(z,t)$ given above, and the values of the static field and saturation induction given in Sec. II.

One important emphasis of the previous section was on the frequency dependences for the v_g and D parameters, and the important effect of these dependences on soliton properties. The η and N parameters, on the other hand, are not particularly sensitive to the small changes in frequency considered here. The η parameter, for example, scales linearly with frequency. On the scale of Fig. 4, the change in η would be about 4%. The N parameter is almost linear in frequency as well, up to 6 GHz or so, and the change in N over the frequencies in Fig. 4 or Table I is only about 3%. These small changes have no effect on the results.

Numerical methods were used to obtain evolved $u(z,t)$ functions as a function of time for z values which correspond to the experimental propagation distance of 4 mm. The logistics of the computations with the NLS equation of Eq. (7) require the use of initial conditions in the form of a spatial pulse of the form $u_0(z,0)$, rather than a temporal pulse as used in the experiments. This $u_0(z,0)$ pulse was taken to have the form

$$u_0(z,0)=\begin{cases}u_{\text{in}}, & |z|\leqslant v_g\Delta T_{\text{in}}/2,\\ 0, & |z|>v_g\Delta T_{\text{in}}/2.\end{cases} \tag{8}$$

The ΔT_{in} parameter corresponds to the 13 ns temporal input pulse width in the experiment. The corresponding width of the spatial pulse used for the modeling is $\Delta Z_{\text{in}}=v_g\Delta T_{\text{in}}$. The u_{in} parameter denotes the amplitude of the input pulse.

Numerical simulations of MME pulse propagation were done based on Eq. (7), with rectangular input pulses of the form given in Eq. (8). The control parameters were the MME pulse group velocity v_g, the dispersion D, the damping parameter η, and the nonlinear response parameter N, as enumerated above, and the input pulse amplitude u_0. Simulations for different operating point frequencies were accomplished by changing v_g and D according to the values in Table I.

The input pulse amplitude u_0 was varied from some very low value around 10^{-3} up to relatively high values of 0.10–0.15. Keep in mind that the u parammeter is a measure of the ratio of the dynamic magnetization amplitude to the saturation magnetization M_s. Values of u_{in} in the 10^{-3} range correspond to a very small dynamic response of about 0.1% of M_s. Values of u_{in} in the 0.10 range correspond to a relatively large dynamic response of about 10% of M_s. The nonlinear effects which lead to soliton properties generally take place when the dynamic magnetization is 1%–10% of M_s. The range of u_{in} values used for the modeling, therefore, extends from small values well into the linear response regime up to large values which are well into the soliton regime.

The purpose of the simulations is to obtain modeling results for comparison with the experimental data given in

the previous section. These data consisted of (i) output pulse power versus time profiles as shown in Fig. 5 and (ii) output pulse peak power P_{out} versus input pulse peak power P_{in} measurements as shown in Fig. 6. For the simulations, the input pulse peak power would be proportional to u_{in}^2. Comparisons between experimental output pulse power versus time profiles and the simulations will require the examination of $|u(z_T,t)|^2$ vs time responses, where z_T denotes the position of the output transducer relative to the input transducer. Comparisons between the experimental P_{out} vs P_{in} profiles and the simulations will require the examination of u_{out}^2 vs u_{in}^2, where u_{out} corresponds to the maximum value of $|u(z_T,t)|$ from the output pulse profile analysis. The precise comparison of u_{out}^2 vs u_{in}^2 profiles with P_{out} vs P_{in} profiles, moreover, will require some kind of calibration between the experimental power P_{in} and u_{in}^2, and between P_{out} and u_{out}^2. Because of the connection between power P and u^2, u^2 parameters will be termed ''power amplitude.''

The numerical simulations were based on the Fourier split step method given in Ref. 21. This method is based on the separation or splitting of the NLS equation into two parts, one linear and one nonlinear. For a given $u_0(z,0)$ initial profile, the linear part can be solved by discrete Fourier transform methods. The solution to the linear part of the NLS equation is then used as an initial condition to step forward the nonlinear part in time and obtain the solution at some time $t=\Delta t$, where Δt is a time step parameter. This solution is then used as the starting point for the next complete cycle to obtain the spatial profile at $t=2\Delta t$, and then at $t=3\Delta t$, and so on.

In this way, the initial $u_0(z,0)$ profile can be stepped forward in time to obtain a series of $u(z,n\Delta t)$ profiles, with $n=1,2,...$, for a range of time $t=n\Delta t$ values which extend from $t=0$ to times beyond the experimental arrival time of the pulse at the output transducer, $t=z_T/v_g$. The spatial step size Δz must be chosen to avoid aliasing effects and to provide an accurate representation of the input signal. For the simulations done here, with a distance scale close to the 4 mm transducer separation and a mesh of 1000 points, Δz is in the 0.004 mm range. The step time Δt is chosen to be small enough to give good convergence and small enough to yield a manageable computation time on a standard personal computer. For the simulations done here, with a time scale of 100 ns or so and a mesh of 1024 time points, Δt is in the range of 0.1 ns. This time step, in combination with the spatial step size Δz indicated above, gave good convergence. Although not reported here, additional simulations were done based on finite difference[19] and Ablowitz–Ladic[20] methods. These results were in good agreement with the results based on the Fourier split step analysis outlined above.

The set of $u(z,n\Delta t)$ profiles were then processed in three steps. First, these functions of z at fixed t were used to construct a $u(z_T,t)$ profile as a function of t at position $z=z_T$. Then, the $u(z_T,t)$ profile was Fourier transformed in the frequency domain to obtain a frequency profile $\mu_{FT}(z_T,\delta\omega)$, where $\delta\omega$ denotes the frequency shift from the operating point frequency ω. Finally, the $\mu_{FT}(z_T,\delta\omega)$ response is adjusted to reflect the characteristic MSW frequency response transmission curve shown in Fig. 2 and the resulting $\mu_{FT}(z_T,\delta\omega)$ response is converted back to a modified $u(z_T,t)$. This filtering process takes the MSW frequency response characteristics into account in determining the final output pulse response obtained from the analysis. This filtering process will be implemented by normalizing the transmission curve of Fig. 2 to the maximum transmission at 5.00 GHz. This means that $\mu_{FT}(z_T,\delta\omega)$ frequency components below or above this point will have a reduced contribution to the reconstructed $u(z_T,t)$ profile after filtering.

As will be seen shortly, filtering will serve to reduce the size of u_{out}^2 by a factor of 2–3. Apart from this simple attenuation, filtering is found to affect the shape of the $u(z_T,t)$ response when the operating point frequency is close to the band edge, as for the 5.00 GHz case discussed above. The results to be presented shortly show that without filtering, the computed $u(z_T,t)$ response is artificially narrow and in poor agreement with experiment. With filtering, the computed profiles agree well with the measurements.

The main effect of these filtering corrections is to account for the MSBVW band edge cutoff at 5.06–5.07 GHz evident from Fig. 2. The filtering process essentially excludes those Fourier frequency components in the NLS generated profile which are above this cutoff from the final reconstructed profile. Use of the transmission loss versus frequency response in Fig. 2 also introduces some corrections due to the input and output transducer transfer functions, since the transmission loss curve takes all of these factors into account experimentally.

The above filtering procedure is strictly valid only for low power MSW pulses. It is used here to reconstruct the pulses obtained from the NLS modeling mainly to account for the band edge cutoff in a simple way. It is well known, however, that MSW dispersion curves, band edge positions, and the resulting shape and position of the transmission loss profile will, in general, change with power.[21,22] Strictly speaking, this means that the transmission loss filtering algorithm should be power dependent, should be applied incrementally along the propagation path from input to output, and should include separate transducer transfer functions. Experimentally, however, only the overall transmission loss may be accessed. As will be evident from the results given below, the present approach yields model results which agree well with experiment.

The main motivation for the NLS analysis described above is to obtain model response curves for comparison with experiment. In closing this section, however, it will prove useful to examine some selected modeling results in their own right. These results will serve to demonstrate (i) the significant effect of dispersion on u_{out}^2 vs u_{in}^2 profiles and (ii) the importance of the transmission response filtering and cutoff on individual $|u(z_T,t)|^2$ power versus time profiles. The matter of calibration and comparison with experiment will be considered in the next section.

Figure 7 shows a series of calculated response curves of u_{out}^2 vs u_{in}^2 which demonstrate the effect of the dispersion parameter D on the power response profile. The D values for the curves range from 2000 to 5000 cm^2/rad s, as indicated. The v_g parameter was set at the experimental value shown in Table I for the 4.90 GHz operating point, 3.94×10^6 cm/s.

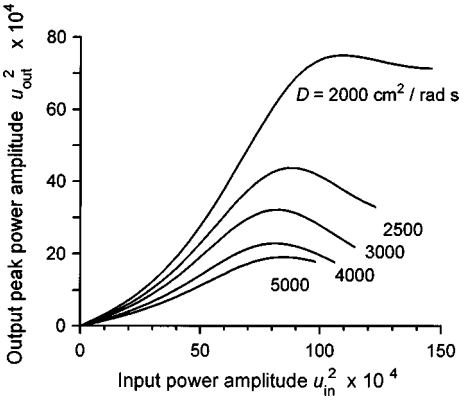

FIG. 7. Calculated response curves of the peak power amplitude response u_{out}^2 vs the peak input power amplitude u_{in}^2 for values of the dispersion parameter D from 2000 to 5000 cm^2/rad s, as indicated. For all of the computations, the group velocity ν_g was set at 3.94×10^6 cm/s, the value corresponding to the 4.9 GHz data, the damping η was set at 7.9×10^6 rad/s, the nonlinear response parameter N was set at 6.85×10^9 rad/s, and the spatial width of the input pulse was set at 0.5122 mm. The output pulse responses were constructed at a position 4 mm from launch.

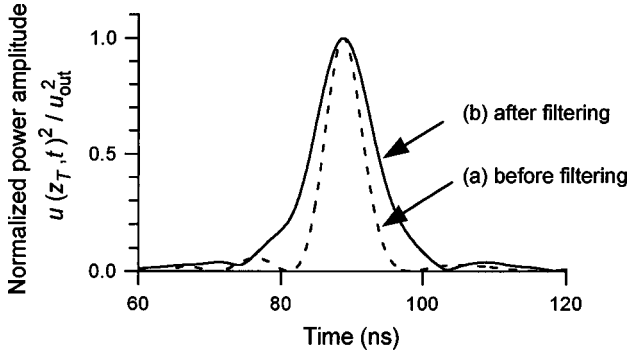

FIG. 8. Calculated power amplitude profiles of $|u(z_T,t)|^2$ vs time, normalized to the peak value of the power amplitude u_{out}^2 in each case. The dispersion parameter D, the group velocity ν_g, the damping η, the nonlinear response parameter N, and the spatial input pulse width were set at 4708 cm^2/rad s, 4.48×10^6 cm/s, 7.9×10^6 rad/s, 6.85×10^9 rad/s, and 0.5122 mm, respectively. The output pulse responses were constructed at a position 4 mm from launch. The D and ν_g parameters correspond to the 5.0 GHz operating point frequency shown in Fig. 4 and Table I. Curve (a) shows the computed profile before filtering and curve (b) includes filtering.

The η and N were assigned the values given above. The spatial width of the input pulse was set at $\Delta Z_{\text{in}}=\nu_g\Delta T_{\text{in}}=0.5122$ mm, based on the experimental temporal input pulse width of 13 ns. The output pulse $|u(z_T,t)|$ response was constructed at $z_T=4$ mm and u_{out} was taken as the maximum value obtained for $|u(z_T,t)|$. These results were obtained with no filtering.

The effect of dispersion on the shape and size of the u_{out}^2 vs u_{in}^2 profile is clear from the curves shown in Fig. 7. For $D=2000$ cm^2/rad s, the u_{out}^2 response is large and the value of u_{in}^2 at which the multisoliton downturn in u_{out}^2 occurs is high. As D is increased from 2000 to 3000 cm^2/rad s, one finds a rapid drop in the size of the u_{out}^2 response. At the same time, the peak in u_{out}^2 becomes more accentuated and shifts to slightly lower values of u_{in}^2. As D is increased further, the size of the response continues o decrease, albeit not so strongly. The peak in u_{out}^2, however, becomes less accentuated and begins to shift to slightly higher values of u_{in}^2. While it is not easily discernable from the low power or low u_{in}^2 region of the graph, the onset of the nonlinear response shifts from $u_{\text{in}}^2\times10^4\approx10$ for $D=2000$ cm^2/rad s to $u_{\text{in}}^2\times10^4\approx20-30$ for $D=5000$ cm^2/rad s. From the definition of the u parameter, this means that the nonlinear onset moves from a peak input dynamic magnetization $|\mathbf{m}|$ value of about 3%–4% of the saturation magnetization at $D=2000$ cm^2/rad s to 4%–6% at $D=5000$ cm^2/rad s.

The rapid change in the u_{out}^2 vs u_{in}^2 response with dispersion shown in Fig. 7 will have an important effect on the modeling results for the soliton data. This change, while somewhat surprising, is completely consistent with the expected effect of D on MME wave packet properties and the nonlinear response associated with solitons. Dispersion, taken alone, causes MME wave packets to broaden and reduce in amplitude. The results in Fig. 7 show that this drop in amplitude occurs even in the presence of nonlinear effects. Keep in mind that soliton formation is usually associated with a steepening and narrowing of the output pulse shape. The results in Fig. 7 show that an increase in D causes a decrease in the steepening.

The increase in the value of u_{in}^2 for the onset of the nonlinear response as D is increased also follows from basic soliton considerations. Considerations based in inverse scattering as well as more qualitative considerations of characteristic dispersion and nonlinear response times[10,20] show that this onset should scale as $\sqrt{D}$. The change in the onset u_{in} value from 3%–4% to 4%–6% of dynamic magnetization $|\mathbf{m}|$ value as ranges from 2000 to 5000 cm^2/rad s is qualitatively consistent with this scaling.

Figure 8 shows representative sets of results on calculated profiles of $|u(z_T,t)|^2$ power amplitude versus time. These profiles were constructed at $z_T=4$ mm. Both of the curves were obtained for $D=4708$ cm^2/rad s and $\nu_g=4.48\times10^6$ cm/s, values corresponding to the 5.0 GHz operating point in Table I. The damping η, the nonlinear response parameter N, and the spatial width of the input pulse were the same as for the Fig. 7 computations. The input power amplitude was set at $u_{\text{in}}^2\times10^4=49$. The curves are shown in a normalized format to facilitate shape comparisons. Curve (a) shows the calculated power amplitude profile obtained if no filtering is applied to the response. Curve (b) shows the profile which is obtained if the transformed frequency spectrum of the curve (a) profile is filtered according to the transmission response of Fig. 2 and then converted back to power amplitude versus time. The unfiltered profile had a peak power amplitude given by $u_{\text{out}}^2\times10^4\approx16$, on the same order as expected from Fig. 7. The filtered profile had a smaller peak power amplitude, down by a factor of about 2.

The key point from Fig. 8 is that the unfiltered profile (a) is narrower than the filtered profile. This difference between the two curves relates to the band edge proximity effects discussed above. Recall that 5.00 GHz is close to the band edge at 5.06–5.07 GHz. Without filtering to take into account the frequency selective properties of the propagating MSBVW signals, one obtains an artificially narrowed output profile response. When the MSBVW transmission response

characteristic is taken into consideration, the pulse response at the output transducer is broader.

The artificial narrowing for calculated MME output profiles occurs when (i) the operating point is close to the MSW band edge, (ii) the MME pulses have a small temporal width and, hence, a wide frequency power, and (iii) there is no filtering process based on the MSW transmission frequency response. These filtering effects have not been previously considered in the evaluation of MME pulse propagation responses through the NLS equation. As Fig. 8 shows, these effects can be very important. They are especially important for solitons because of the steepening and narrowing of the pulse profiles which accompanies soliton formation. The narrower the pulse, the wider the frequency power spectrum, and the more important the filtering through the MSW transmission response. For operating points well away from a band edge, these effects are not as critical.

IV. THE MODELING OF SOLITON DATA

The key to a meaningful comparison of theory with experiment is in the calibration between the measured peak powers P_{in} and P_{out} and the computed peak power amplitude parameters u_{in}^2 and u_{out}^2. Once these calibrations are established, one can make direct comparisons between peak power response curves of the sort shown in Figs. 6 and 7. Based on these calibrations, one can also compare computed $|u(z_T,t)|^2$ profiles with measured pulse profiles of the sort shown in Figs. 3 and 5. For the present purposes, a simple and direct calibration procedure was adopted. In this procedure, it is assumed that the P_{in} and P_{out} values at the peaks evident from the P_{out} vs P_{in} data correspond, respectively, to the u_{in}^2 and u_{out}^2 values at the peaks evident from the computed u_{out}^2 vs u_{in}^2 response curves.

Input and output calibration factors, taken as C_{in} and C_{out}, are defined as the ratios of the peak powers and the corresponding peak power amplitudes according to

$$C_{\text{in}}=\left.\frac{P_{\text{in}}}{u_{\text{in}}^2\times 10^4}\right|_{\max} \tag{9}$$

and

$$C_{\text{out}}=\left.\frac{P_{\text{out}}}{u_{\text{out}}^2\times 10^4}\right|_{\max}. \tag{10}$$

The ''max'' indicates that these factors are evaluated at the maximum P_{out} and u_{out}^2 positions for the measured and computed response curves, respectively.

The results from Secs. II and III may be used establish rough values for C_{in} and C_{out} applicable to the current measurements and modeling. Consider, for example, the 4.90 GHz peak power response data in Fig. 6 and the $D=2500\ \text{cm}^2/\text{rad s}$ power amplitude response in Fig. 7. From these results, one has $P_{\text{in}}\approx 250-300$ mW, $P_{\text{out}}\approx 2$ mW, $u_{\text{in}}^2\times 10^4\approx 80-90$ and $u_{\text{out}}^2\times 10^4\approx 40-50$. These values yield C_{in} and C_{out} values of about 3 and 0.05 mW, respectively.

Note that the results shown in Fig. 7 are without filtering. Filtering reduces u_{out} and, hence, will serve to increase C_{out}. Table II summarizes the actual values obtained for C_{in} and C_{out} for all three of the frequency operating points used for the measurements. These values are based on the data shown in Fig. 6 and u_{out}^2 vs u_{in}^2 response curves similar to those shown in Fig. 7 but for the experimental values of D and ν_g listed in Table I. Values are shown with and without filtering. Filtering has only a small effect on C_{in}. Filtering serves to increase C_{out} by a factor of 2–3.

TABLE II. Power–power amplitude calibration factors C_{in} and C_{out} for the modeling of soliton data without and with transmission filtering at the three operating point carrier frequencies.

Frequency		4.90 GHz	4.96 GHz	5.00 GHz
Without filtering	C_{in}	3.298	4.218	5.499
	C_{out}	0.0596	0.0958	0.113
With filtering	C_{in}	3.374	4.218	5.263
	C_{out}	0.169	0.203	0.236

Based on the calibration parameters given above, it is now possible to make direct comparisons between the measurements and the modeling results. These comparisons will be made by converting the u^2 power amplitude parameters to powers according to Table II. Three specific comparisons are shown below. Figure 9 compares computed curves of the output peak power amplitude u_{out}^2 vs input power amplitude u_{in}^2 with the experimental results on output pulse peak power P_{out} vs input pulse peak power P_{in}. Comparisons are made for all three sets of experimental results shown in Fig. 6. Figures 10 and 11 show comparisons for computed and measured output profiles. Figure 10 compares profiles for the 4.90 GHz operating point frequency, the operating point which is away from the band edge. Figure 11 compares pro-

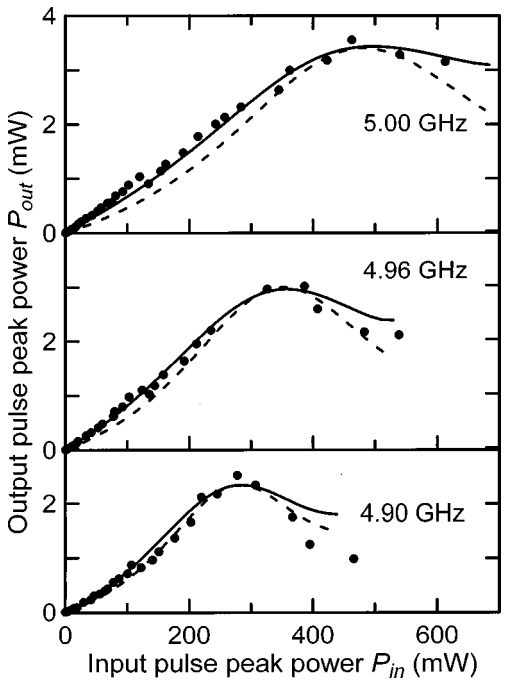

FIG. 9. Solid points show the data on output pulse peak power P_{out} vs input pulse peak power P_{in} from Fig. 6 for the same three operating point frequencies, as indicated. The solid and dashed curves show the results of the modeling with and without filtering, respectively. These curves are based on the NLS equation, the operating point parameters in Table I, the calibration parameters in Table II, and the same 4 mm propagation distance and 13 ns pulse width as used in the measurements.

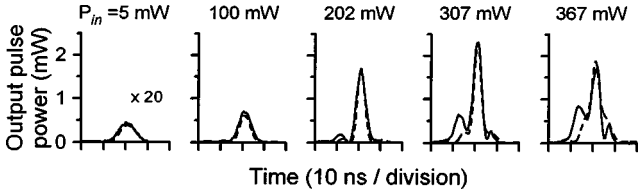

FIG. 10. Solid and dashed curves show measured and computed output power vs time profiles, respectively, for the indicated input pulse peak power P_{in} values. The parameters were the same as for the bottom graph in Fig. 9 and the 4.90 GHz operating point frequency. The computed curves were obtained with no filtering.

files for 5.00 GHz, the operating point which is close to the band edge. For Fig. 11, the comparison computed curves are shown with and without filtering.

First consider the P_{out} vs P_{in} response. The discussion of Fig. 6 pointed out the change in the shape of the P_{out} vs P_{in} response as one moves closer to the band edge. There were two main effects. First, the onset of the nonlinear response moves to higher powers. Second, there was an amelioration in the nonlinear change and in the general concave upward shape of the onset response. As pointed out in connection with the results in Fig. 7, the shift to higher powers is due to the increase in the dispersion. The amelioration in the onset response is due to band edge filtering.

Both effects are clearly evident from the modeling results which have been added to the data in Fig. 9. The solid points in Fig. 9 repeat the three sets of P_{out} vs P_{in} data from Fig. 6 for 4.90, 4.96, and 5.00 GHz. The solid and dashed lines show the computed u_{out}^2 vs u_{in}^2 results obtained with and without filtering, respectively, after conversion from power amplitude to power according to Table II.

The match up between the NLS modeling results and the P_{out} vs P_{in} data is remarkable. At 4.90 GHz, the frequency farthest from the band edge, the filtered response shown by the solid curve and the unfiltered response shown by the dashed line are about the same and follow the data reasonably well. As one moves closer to the band edge, as for the 4.96 and 5.00 GHz results, the filtered model response follows the change in the data while the unfiltered model response does not. For 5.00 GHz, the filtered model response closely follows the data both below and above the peak in

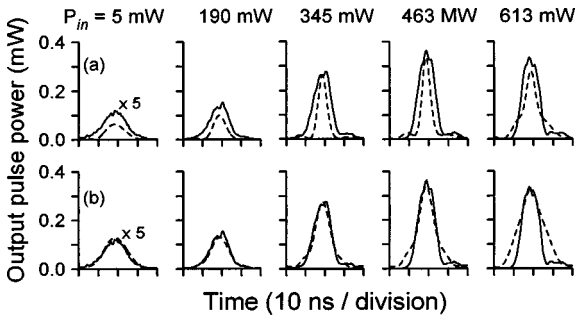

FIG. 11. Solid and dashed curves show measured and computed output power vs time profiles, respectively, for the indicated input pulse peak power P_{in} values. The parameters were the same as for the top graph in Fig. 9 and the 5.00 GHz operating point frequency. The computed curves in the bottom and top series of diagrams were obtained with and without filtering.

P_{out}. The problem with the dashed line response is clear. These curves, obtained with no filtering to account for the frequency response of the MSW signal, show only a small change in the onset as one moves from 4.90 to 4.96 GHz, and then to 5.00 GHz. All three dashed line curves show a distinct concave upward nature in the 0–200, 0–300, and 0–400 mW input power range, respectively. The expansion in input power is related to the increase in the dispersion parameter D as one moves from 4.90 to 5.00 GHz.

The crucial change which results from the filtering process is evident from the solid curves. With filtering, the concave upward shape of the computed 4.90 GHz result is changed only slightly. Both the solid and the dashed curves provide a good match with the data. For 4.96 GHz, the concave upward character of the computed response curve for no filtering is now reduced. Here, it is clear that the best fit to the data occurs for the solid curve, obtained with the application of filtering. The situation is even clearer for 5.00 GHz. Here, the dashed line model result for no filtering falls well away from the data, while the solid line calculation with filtering matches the data quite well. These results demonstrate the critical effect of filtering, and the importance of the MSW frequency response in the analysis.

Now turn to a comparison of actual pulse profiles. Figures 10 and 11 show comparisons of experimental and computed output pulse profiles of power versus time for 4.90 and 5.00 GHz, respectively. Recall that the 4.90 GHz operating point frequency is relatively far from the band edge where filtering effects are not critical, as for the bottom graph in Fig. 9. The 5.00 GHz operating point is close to the band edge and filtering effects are important, as in the top graph of Fig. 9. The solid curves in both figures show a series of experimental profiles of output pulse power versus time obtained for a sequence of increasing P_{in} values, as indicated. The dashed lines show computed profiles. In Fig. 10, the computed profiles were obtained without filtering. Because 4.90 GHz is far from the band edge, the same curves obtained with filtering are not substantially different. Figure 11 shows two series of profiles. The experimental solid line profiles are the same for both. The dashed curves in the bottom and the top series are with and without filtering, respectively. All the computed curves are based on the parameters listed in Tables I and II. No additional fitting was needed to obtain the results shown.

The good agreement between the model profiles and the data are evident from both figures. In Fig. 10, the central peak regions of the data are well matched by the calculated profiles. The NLS analysis does not give a perfect match for the experimental side lobes, but even here, the model profiles give some indication of these features. The most important aspect of the match is in the steepening and narrowing which occurs with an increase in power.

Figure 11 provides a further demonstration of the band edge effects for frequencies close to the MSBVW cutoff. The dashed line calculated profiles in the top series of graphs show that without filtering the theoretical curves are generally steeper than shown by the data. When filtering is included, however, the calculated curves broaden out just enough to mimic the data. Notice that the narrowing shown

by the data in Fig. 10, a far-from-the-band-edge situation, is much more accentuated than for Fig. 11.

These results show that the accurate modeling of MME soliton data requires attention to two important points, (i) the use of accurate magnetic parameters and (ii) attention to filtering due to the MSW response. When these points are accommodated, one may obtain accurate fits of the NLS theory to the experiment.

It is important to note that the good fit of the theory to the data does not extend to the highest powers. Some of the high power experimental points in Fig. 9 match the theory and some do not. The right most theoretical profiles in Fig. 10 and the bottom part of Fig. 11 deviate somewhat from the data. Recent measurements in this high power regime by Brillouin light scattering[23] (BLS) indicate that the nonlinear response is accompanied by the generation of high wave number spin waves and that there is a substantial amount of additional energy going into these spin waves from the elemental soliton mode. The microstrip antenna is unable to pick up the spin wave power, so that the profile detected by the antenna does not represent the total response. Similarly, the NLS equation based model does not explicitly include spin wave processes. Further progress in the theoretical analysis for the regime of very high powers will require (i) a combination of microwave and BLS measurements to fully define the magnetic excitation spectrum associated with the soliton, (ii) additional theory to model high power soliton properties which includes higher order nonlinear terms in the NLS equation, and (iii) modifications of the theory to include energy flow into spin waves.

V. SUMMARY AND CONCLUSIONS

A critical study of MME soliton profiles and the soliton peak power response has been accomplished. This study was based on computed soliton properties obtained from the standard nonlinear Schrödinger equation with all the key parameters based on experiment. The use of accurate dispersion and group velocity parameters were particularly critical. It was also necessary to take the transmitted power versus frequency response of the MSW excitations into account, especially when the operating point frequency is close to the band edge. The above study has provided new insight and new confidence for the application of the NLS equation to the modeling of experimental microwave magnetic envelope soliton properties. The discrepancies apparent from previous attempts at such modeling have been resolved.

Further work is needed to define valid modeling procedures at very high power levels. In this regime, well above the maximum in the peak power response, it may be necessary to include higher order terms in the NLS equation and introduce additional channels of energy flow into spin waves.

ACKNOWLEDGMENTS

This work was supported by the National Science Foundation, Grant No. DMR-9400276, the United States Army Research Office, Grant No. DAAHO4-95-1-0325, and the Slovak Science Foundation, Grant No. 1/9288/97. Mr. Reinhold Staudinger was supported in part by the Deutscher Akademischer Austauschdienst (DAAD). The samples were provided by Dr. J. Douglas Adam, Northrop Grumman Science and Technology Center, Pittsburgh, Pennsylvania. Professor Yuri K. Fetisov is acknowledged for helpful discussions about the importance of the transmission versus frequency response in the computed MSW pulse response.

[1] A. Hasegawa, *Optical Solitons in Fibres* (Springer, New York, 1990), pp. 1–3 and 17.
[2] B. A. Kalinikos, N. G. Kovshikov, and A. N. Slavin, JETP Lett. **38**, 413 (1983).
[3] B. A. Kalinikos, N. G. Kovshikov, and A. N. Slavin, Sov. Tech. Phys. Lett. **10**, 392 (1984).
[4] A. D. Boardman, G. S. Cooper, A. A. Maradudin, and T. P. Shen, Phys. Rev. B **34**, 8273 (1986).
[5] P. De Gasperis, R. Marcelli, and G. Miccoli, Phys. Rev. Lett. **59**, 481 (1987).
[6] B. A. Kalinikos, N. G. Kovshikov, and A. N. Slavin, Sov. Phys. JETP **67**, 303 (1988).
[7] B. A. Kalinikos, N. G. Kovshikov, P. A. Kolodin, and A. N. Slavin, Solid State Commun. **74**, 989 (1990).
[8] M. Dragoman and D. Georgescu, Appl. Phys. Lett. **59**, 1788 (1991).
[9] M. Chen, J. M. Nash, and C. E. Patton, J. Appl. Phys. **73**, 3906 (1993).
[10] M. Chen, M. A. Tsankov, J. M. Nash, and C. E. Patton, Phys. Rev. Lett. **70**, 1707 (1993).
[11] M. Chen, M. A. Tsankov, J. M. Nash, and C. E. Patton, Phys. Rev. B **49**, 12773 (1994).
[12] M. A. Tsankov, M. Chen, and C. E. Patton, J. Appl. Phys. **76**, 4274 (1994).
[13] A. D. Boardman, A. N. Nokitov, K. Xie, and H. Mehta, J. Magn. Magn. Mater. **145**, 357 (1995).
[14] J. M. Nash, C. E. Patton, and P. Kabos, Phys. Rev. B **51**, 15079 (1995).
[15] X. Hua, P. Kabos, C. E. Patton, and H. E. Ensle, Phys. Rev. B **55**, 15018 (1996).
[16] A. N. Slavin, Phys. Rev. Lett. **77**, 4644 (1996).
[17] L. H. Li, K. Yashiro, S. Ohkawa, C. E. Zaspel, and A. N. Slavin, IEEE Trans. Magn. **33**, 3442 (1997).
[18] M. J. Ablowitz and P. A. Clarkson, *Soliton, Nonlinear Evolution Equations and Inverse Scattering* (Cambridge University Press, Cambridge, 1991), p. 1.
[19] R. A. Standinger, P. Kabos, H. Xia, B. T. Faber, and C. E. Patton, IEEE Trans. Magn. **34**, 2334 (1998).
[20] T. R. Taha and M. J. Abolowitz, J. Comput. Phys. **55**, 203 (1984).
[21] M. A. Tsankov, M. Chen, and C. E. Patton, J. Appl. Phys. **79**, 1595 (1996).
[22] A. Prabhakar and D. D. Stancil, Phys. Rev. B **57**, 11483 (1998).
[23] H. Xia, P. Kabos, H. Y. Zhang, P. A. Kolodin, and C. E. Patton, Phys. Rev. Lett. **80**, 449 (1998).